Journal of the European Ceramic Society 45 (2025) 117039

Contents lists available at ScienceDirect

Journal of the European Ceramic Society

journal homepage: www.elsevier.com/locate/jeurceramsoc

Detailed study of interphase degradation in SiC/BN/SiC ceramic matrix composites after elevated temperature tensile testing

L.R.M. Toller-Nordström [a,*], O. Gavalda-Diaz [b], L. Gale [c], D.E.J. Armstrong [a], R.J. Nicholls [a]

[a] Department of Materials, University of Oxford, Oxford OX1 3PH, UK
[b] Department of Materials, Imperial College London, London SW7 2AC, UK
[c] Rolls Royce plc., Derby DE24 8BJ, UK

ARTICLE INFO

Keywords:
Ceramic matrix composites
Electron energy loss spectroscopy
Environmental degradation
Silicon carbide
Hexagonal boron nitride

ABSTRACT

Ceramic matrix composites of silicon carbide fibres in a silicon carbide matrix with boron nitride interphase are promising candidates for replacing superalloys in the hottest part of aerospace engines, reducing the need for cooling and increasing the fuel efficiency. This needs a thorough understanding of how these materials degrade under high levels of stress combined with high temperatures in an oxidative environment. This work presents a detailed investigation of the degradation in the interphase and surrounding interfaces. Advanced electron microscopy and electron energy loss spectroscopy are used to extract information on the degradation process. It was found that silica and boria form along with a migration of silica into the interphase. At 1000 °C the degradation along the surface leads to early fracture at the surface and eventually complete fracture of the composite, lower temperature allows for the oxidation to reach the centre of the sample before complete failure.

1. Introduction

Ceramic matrix composites (CMCs) with silicon carbide, SiC, fibres in a SiC matrix can provide a unique combination of high temperature hardness and sufficient resistance to brittle fracture and are therefore considered for use in applications such as jet engines and nuclear reactors [1]. This work studies materials intended for jet engine applications, where replacing currently used nickel superalloys with CMCs would permit raising the engine temperature, reducing the need for cooling and increasing the fuel efficiency [2–4]. To be able to implement CMCs on a broader scale it is crucial to understand the degradation at elevated temperature in oxidative environment. This work contributes to this understanding by providing an in-depth analysis of degraded samples.

The principle behind fibre reinforced CMC's is to enable artificial ductility above the onset of cracking, where the material would otherwise undergo fracture and catastrophic failure. This is done by allowing cracks to deflect along the fibre/matrix interface instead of traversing the fibres, leading to a longer overall crack path. Once the fibres do fracture, the fibre fracture plane is likely not in line with the matrix fracture plane, leading to friction forces from fibre pull-out [5–7]. In combination, this gives higher resistance to fracture and more graceful failure.

Crack deflection is enabled via replacing the interface by an interphase material with a low fracture energy but good adhesion to the fibre and matrix [8]. Both pyrolytic carbon and hexagonal boron nitride, hBN, have been used for this [9]. In aerospace applications hBN is commonly preferred because of its liquid oxide, compared to pyrolytic carbon which instead has gaseous reaction products known to lead to annular voids around the fibres [8,10].

Elevated temperature and oxidative environments lead to degradation of CMC's through oxidation of SiC and BN. Silicon carbide will oxidise preferentially before BN and act as an oxygen getter [11–13], forming silica according to [14]:

$$SiC(s) + \frac{3}{2}O_2(g) \longrightarrow SiO_2(s) + CO(g) \quad (1)$$

or [8]:

$$SiC(s) + 2O_2(g) \longrightarrow SiO_2(s) + CO_2(g) \quad (2)$$

In environments where the oxygen levels are low in relation to the oxidation rate, it is also possible for silica to oxidise with solid carbon as a by-product by [11]:

$$SiC(s) + O_2(g) \longrightarrow SiO_2(s) + C(s) \quad (3)$$

SiC oxidation will eventually be controlled by the oxygen diffusion through the formed silica layer, which will form a passivating layer

* Corresponding author.
E-mail addresses: lisa.toller-nordstrom@materials.ox.ac.uk (L.R.M. Toller-Nordström), rebecca.nicholls@materials.ox.ac.uk (R.J. Nicholls).

https://doi.org/10.1016/j.jeurceramsoc.2024.117039
Received 24 September 2024; Received in revised form 22 October 2024; Accepted 29 October 2024
Available online 6 November 2024

on the SiC [14]. At temperatures up to 1000 °C the silica formed is expected to be amorphous [15,16].

BN will oxidise to form boria according to [17]:

$$2BN(s) + \frac{3}{2}O_2(g) \longrightarrow B_2O_3(l) + N_2(g) \quad (4)$$

Boria can mix with the silica to form a borosilicate glass [18]. Even at small boria fraction, borosilicate glass has a significantly lower viscosity and lower glass transition temperature compared with pure silica glass [19,20]. The glass transition temperature of a 50–50 mixture of silica and boria is between 300 and 350 °C [20], which is much lower than that for pure silica at 1190 °C [21]. Also at much lower boria content a significant reduction in glass transition temperature is expected. The oxygen transport through liquid borosilicate glass is much quicker than through solid silica, thus the presence of boron containing compounds can lead to an increased oxidation of the fibre and matrix [12,22–24]. This is sometimes used as an argument against the use of BN interphases, but the benefit of the liquid oxide is that it may also flow to fill pores and cracks, thereby having a healing effect in preventing direct contact with the oxygen in the atmosphere [25,26]. The total effect of the presence of BN on SiC oxidation may therefore vary throughout the material by increasing the oxygen transport in some areas and preventing it in other.

In the presence of water vapour, volatilisation of boria will happen through the formation of HBO_2 or H_3BO_2 via for example [12,17]:

$$B_2O_3(l) + H_2O(g) \longrightarrow 2HBO_2(g) \quad (5)$$

The rate of volatilisation is typically controlled by the transport of B-containing gasses away from the site of reaction, which in turn will depend on the proximity to the surrounding atmosphere [26]. This will cause a depletion of boria in the borosilicate glass and thus an increase in viscosity, and eventually the glass will solidify. At this stage the interphase will be entirely or in part replaced by a solid glass which can be strongly bonded to the fibres, which will not allow for crack deflection and can give brittle fracture of the whole composite. Silica may also volatize, but does so at a significantly lower rate than boria [14,27].

Depending on the temperature during deposition, the BN interphase could have different levels of crystallinity. The basic structure is in the form of sheets with hexagonal structure, in its fully crystalline shape the sheets are ordered in a 3-dimensional layered structure [28], analogous to graphite. At lower depositions temperature the BN still forms sheets and layered structure but the 3-dimensional ordering is lost and the material will have smaller layered grains with random orientation and regions of amorphous structure, this is known as turbostratic BN, tBN [6,28]. The crystallinity of the BN interlayer will affect its resistance to oxidation, with increased crystallinity leading to increased oxidation resistance [17,28].

The degradation of SiC/BN/SiC CMCs have been studied at temperatures ranging between room temperature and 1200 °C and in different environments, including air [29–32], combustion environment [13,33,34] and water vapour [23,30,31]. Common conclusions are that the main oxidation products detected are the ones formed by reaction (1) to (5) and in particular the interfaces appear especially susceptible to oxidation [13,23]. The amounts of oxidation increase with increasing time and temperature which leads to lower tensile strength and less fibre pull-out on fracture surfaces [32,35,36]. Burner rig tests with simulated combustor environment have also been found to be more detrimental than testing in laboratory air [33,36]. If the sample is subjected to sufficient tensile stress, somewhere between 100 and 200 MPa for most samples [1,37], microcracks form in the matrix allowing for faster oxygen transport deeper into the material and to the fibre/interphase/matrix region, leading to uneven oxidation that follows the crack network [13]. Especially detrimental is the combination of an oxidative environment and tensile stress that can induce cracking [33]. It is further common to find that the oxidation is limited by diffusion [12]. Some studies find clear signs of liquid flowing oxide and void formation from gaseous reaction products [23,29].

Comparing different studies in detail is complicated due to the use of different fibres and different methods for densification of the matrix. Early fibre types typically contained oxygen and were thus more susceptible to oxidation [38–40] and some methods of densification will lead to significant amounts of pores in the matrix [32,41,42].

Much work on degradation of CMC's have been carried out in tension–tension fatigue tests at different environments [29,32,33]. In this work the samples are instead tested in tensile creep under constant tensile stress at elevated temperature and in air, to simulate the situation for parts at a constant or semi-constant stress state. The temperatures tested, 1000, 600 and 400 °C are relevant for components close to the combustion in an airplane jet engine. Here we use advanced electron microscopy and electron energy loss spectroscopy to give a detailed account of the oxidation, including local changes in chemistry, at the fibre/interphase/matrix interfaces to contribute to the understanding of how these composites degrade.

Table 1
Test parameters from tensile creep tests.

Name	Temp. [°C]	Max appl. stress [MPa]	Time to failure [h]
CMC1000	1000	193	27.34
CMC600	600	193	150.11
CMC400	400	193	2426.0

2. Methods and materials

2.1. Ceramic matrix composites

The samples used in this study were supplied by Rolls Royce plc. High Temperature Composites. They were made from woven sheets with tows of Hi Nicalon silicon carbide fibres (NGS Advanced Fibers Co., Ltd, Japan) in a satin weave. The fibres were coated by chemical vapour infiltration, first with a layer of tBN interphase and then with a first matrix of SiC, the first will be referred to as the "interphase" and the latter will be referred to as "CVI SiC" in this work. Multiple woven sheets were stacked together and melt infiltrated with silicon to produce a relatively dense sample. From this the final dog-bone shape was cut, see Fig. 1(a).

2.2. Tensile creep tests

Tensile creep tests were performed in air at three different temperatures given in Table 1. The maximum applied stress was 193 MPa in all the tests, which should be high enough to initiate matrix cracking [1,37]. All samples were tested until failure. Due to long hold times for some of the samples, only one sample was tested at each set of conditions.

2.3. Sample preparation for analysis

The sectioning of the fractured samples can be seen in Fig. 1(b). The piece labelled 1 in Fig. 1(b) was sectioned with an oil cooled slow speed saw and glued straight onto an SEM stub by using silver dag with the sample surface up. The pieces labelled 2 and 3 in Fig. 1(b) were sectioned by a water cooled high speed saw.

2.3.1. Polished cross-sections

The cross section polishing was done on the sample piece labelled 3 in Fig. 1(b). Traditional metallographic polishing was used but using lubricants and suspensions free from water to avoid oxidation during sample preparation. First, the samples were polished on polishing discs with embedded diamond particles corresponding to 80, 120 and 300 grit SiC paper. This was followed by three steps using diamond suspensions on cloth, 9 μm, 3 μm and 1 μm. Final polishing was done with a suspension with 0.25 μm colloidal silica on cloth.

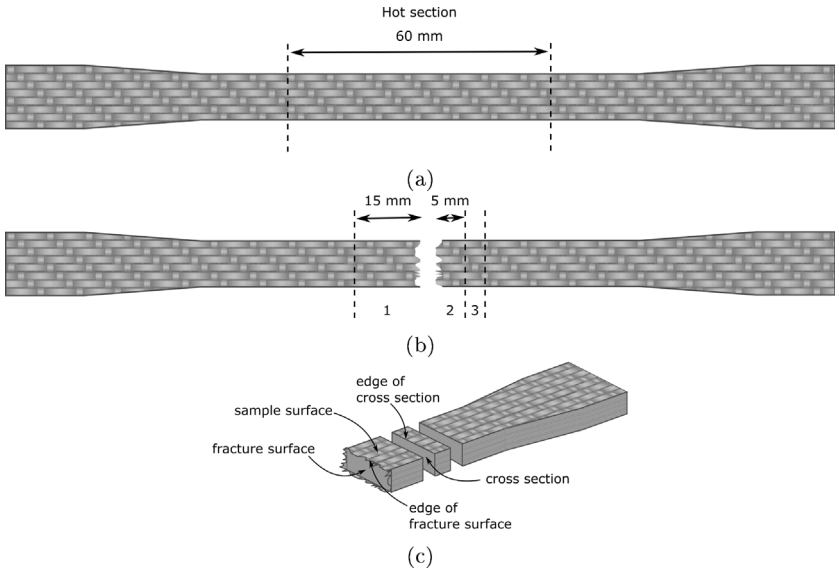

Fig. 1. Dogbone samples used in the tensile creep test. (a) Original sample geometry. (b) Failed sample, showing the sectioning of samples to be viewed from the surface (1) and the sample polished as a cross-section (3). (c) The naming convention for the different areas of the samples described in the text.

2.3.2. TEM-samples

All TEM-lamellae were made using a Zeiss Auriga dual-beam focused ion beam and scanning electron microscope, FIB-SEM. If nothing else is stated the microscope was operated with the ion gun at 30 kV acceleration voltage and the electron gun at 5 kV acceleration voltage. "Surface samples" were lamellae extracted perpendicular to the exposed surface during the test, labelled "sample surface" in Fig. 1(c). This was done approximately 0.5 mm from the fracture surface on the sample piece labelled 1 in Fig. 1(b) which was glued onto the SEM sample stub. These samples contain cross sections through the fibres and interphases closest to the environment during testing. "Centre samples" were produced from the centre of a fibre tow in the centre of the polished cross sections of piece 3 in Fig. 1(b), these fibres and interphases require the oxidising species to travel the longest inside the hot-zone.

Samples were produced as lift-outs using the ion beam to cut a lamella and a Kleindiek needle to move the lamella to a copper 3-post grid. The thinning was done in multiple steps at a slight over-tilt, with final steps at 15 kV, 250 pA to get down to electron transparency, and a final step at 5 kV, 240 pA to remove surface damage caused by higher acceleration voltage.

To reduce contamination during the subsequent analysis, the lamella samples were heated under vacuum. The heating was done either for 24 h at 95 °C in a plasma cleaning rig without any plasma, or for 48 h at 100 °C in a vacuum baking rig. The surface samples were analysed also before the heating was carried out and no changes in crystallinity or chemistry were found when comparing samples before and after heating.

2.4. Electron microscopy

2.4.1. Scanning electron microscopy

To get an overview of the degradation, scanning electron microscopy, SEM, using secondary electrons was used to image both fracture surfaces and polished surfaces. Fracture surfaces images were from the piece labelled 2 in Fig. 1(b) and imaged in a dual beam Zeiss Auriga FIB-SEM operated in SEM mode, operated at 5 kV. Due to a limited field of view the images were stitched together to view the entire fracture surface. The polished surfaces of sample piece 3 in Fig. 1(b) were imaged at an acceleration voltage of 10 kV.

2.4.2. Transmission electron microscopy

Transmission electron microscopy, TEM, was used for creating overview images of the surface samples. This was done in bright field mode by acquiring overlapping images that were subsequently stitched together in an image processing software. The crystallinity of different phases was determined by selected area diffraction, SAD, and high resolution TEM, HR-TEM. For SAD an aperture with a diameter of 350 nm was used. The TEM used in this study was a JEOL 2100 with a LaB_6 filament operated at 200 kV.

2.4.3. Electron energy loss spectroscopy

Electron energy loss spectroscopy, EELS, was acquired alongside scanning transmission electron microscopy, STEM, imaging with a high-angle annular dark field, HAADF, detector. This was done in a probe corrected JEOL 200F ARM with a cold FEG operated at 200 kV.

The system used for EELS acquisition was a Gatan GIF Quantum 965 ER, capable of performing dual-EELS. All data was acquired in the form of maps, with step size and pixel dwell time varying to achieve desired resolution, reasonable contamination and/or reasonable acquisition times. The camera length was set to 2 cm and the system was operated with a 5 mm entrance aperture. Two different energy dispersions were used, 0.25 eV/channel, giving a spectra spanning over 500 eV was used to include edges from all elements in a single map and 0.1 eV/channel spanning over 200 eV was used to study the near edge fine structure. All maps were acquired in dual-EELS mode with one of the acquired spectra being the zero-loss peak. All EELS acquisition suffered from correlated noise in the detector. Steps were taken to minimise this but it was not possible to eliminate it completely.

Post-processing of EELS data was done in HyperSpy and included steps of spike removal, alignment of spectra with the zero loss peak and background removal by fitting a polynomial to the signal before individual edges. Some spectra had background removal done in Digital Micrograph, where it is possible to use more than one window for the background fitting. This was needed for some edges of low intensity due to the correlated noise, uneven sample thickness and in some cases edge overlaps. Spectra used to analyse the fine structure were obtained by binning multiple pixels acquired in the same phase, all these spectra were normalised by the size of the binned region. Elemental maps were produced in Digital Micrograph.

Boron in the form of boria or borosilicate can be separated from turbostratic boron nitride by the shift of the edge onset, which is about 1.5 eV higher for boria/borosilicate than for sp^2-hybridised boron in the hexagonal sheets of hBN or tBN.

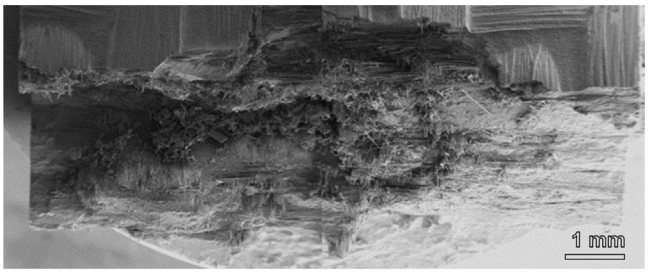

(a) CMC1000

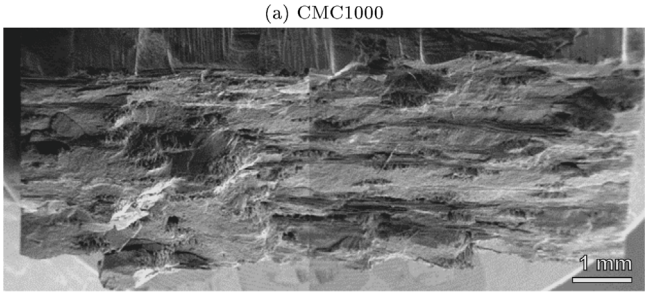

(b) CMC600

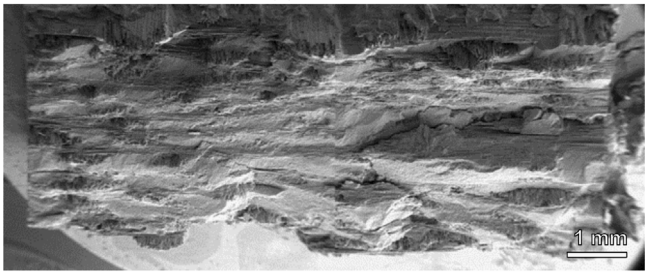

(c) CMC400

Fig. 2. SEM images of the fracture surfaces from the tensile creep test. The top of the images show the edge of the fracture surface and a small section of the sample surface which was exposed during the test.

3. Results

The time to failure experienced by the samples tested at different temperature can be found in Table 1, and it can be seen that it varies with over two orders of magnitude. Higher temperature lead to shorter test times in line with what can be expected [36,43].

3.1. Fracture surfaces

SEM imaging of the fracture surfaces reveals fractured fibres and fibre pull out, see Fig. 2. The amount of fibre pull-out varies between samples, with less fibre pull out in the samples tested at lower temperature and longer time until fracture. The sample tested at 1000 °C has very minimal fibre pull out along the edges, as can be seen by the fibres having fractured at a plane close to that of the matrix, and fibre pull out across the internal regions of the sample, see Fig. 2(a). This type of "picture frame" degradation has been seen before and is attributed to early degradation along the surface, leading to cracks propagating also through the fibres due to changed interface and interphase properties. The remaining fibres cannot withstand bearing the load and the sample fractures, but with fibre pull out in the centre where the interphase is still close to the as-manufactured state and deflects cracks as intended [32,42,44].

The sample tested at 600 °C has less fibre pull out of shorter fibres, again with fibres fractured close to the matrix plane dominating around the edges, see Fig. 2(b). Finally, the sample tested at 400 °C has almost exclusively fibre fracture close to the matrix fracture plane all across the fracture surface, and minimal fibre pull out, see Fig. 2(c). Thus, in the sample tested at 400 °C the early degradation along the surface did not lead to significant fibre fracture and transfer of load, instead the degradation was allowed to penetrate the entire sample before significant fibre fracture occurred, leading to more or less complete loss of the crack deflecting properties of the interphase.

The fracture surfaces highlights the importance of understanding how the interphase and interfaces change during the test, and this work will therefore continue the investigation down to the nanoscale.

3.2. Polished cross sections

The polished cross sections show that in the centre, the microstructure of the CMC1000 sample looks very similar to a pristine one [26,33] with even contrast in the interphase, see Fig. 3(b), the CMC600 sample has some variations in contrast in the interphase, see Fig. 3(d), and finally the CMC400 sample has both uneven BN interphase and fractured fibres, see Fig. 3(f). In images acquired at the cross section edge, all samples show uneven boron nitride interphase as well as cracks and chipping in the SiC fibres, which both are indications of degradation of the interphase and fibres. The uneven contrast of the BN interphase and the chipping of fibres as seen in Fig. 3 can only be interpreted as an indication of degradation, rather than a confirmation. As such it tells the same story as the fracture surfaces, namely that at the higher temperatures failure happened before the degradation could reach the centre, while the samples tested at lower temperature had time for transport of oxidising agents also to the centre. The investigation of the TEM-lamella will provide details and confirm this.

3.3. (S)TEM surface samples

Overview images of the electron transparent region of all surface samples can be seen in Fig. 4. Samples CMC600 and CMC400 have cracks between fibre and interphase, indicative of inside debonding. They were present already during the early stages of sample preparation and not caused by the ion milling. The following will focus on the interphase as well as the interfaces between fibre and interphase and CVI SiC and interphase.

The crystallinity of the interphase was determined by SAD and HR-TEM and it was seen that all samples have turbostratic BN as the main interphase constituent, see Figures S1 to S6 in the Supplementary Information. This shows that even at the edge of the samples, the part with the highest exposure to the oxidating species, and at the point of failure, the majority of the remaining interphase is still tBN. The uneven contrast seen by SEM in the polished cross sections can therefore be interpreted as partial oxidation of the interphase, and the early failure of fibres and loss of fibre pull out along the edges cannot be attributed to complete oxidation of the interphase.

3.3.1. Oxide layers

From the elemental maps produced by EELS analysis, see maps in Fig. 5, it is possible to see that all surface samples have oxide layers at the fibre/interphase interface, or in the case of a crack separating the fibre and interphase the oxide is at the fibre surface. The thickness of the oxide layer increase with temperature, approximately 20 nm for sample CMC400, 80 nm for sample CMC600 and 20 to 200 nm for sample CMC1000.

It is evident that the oxide layers differ between CMC1000 and the other two samples, where the former has oxide layers on both fibre and CVI interfaces, see oxygen maps in Fig. 5(a) and in Figure S8 in the Supplementary Information, and the latter have oxide layers on only the fibre, see Fig. 5(b) and Figures S9 and S10 in the Supplementary Information for CMC600 and 5(c) for CMC400. The oxidation seems to have been especially severe in the area where the two fibres are separated by only interphase in CMC1000, where the oxide layers following the fibre/interphase interface form a bridge that joins the

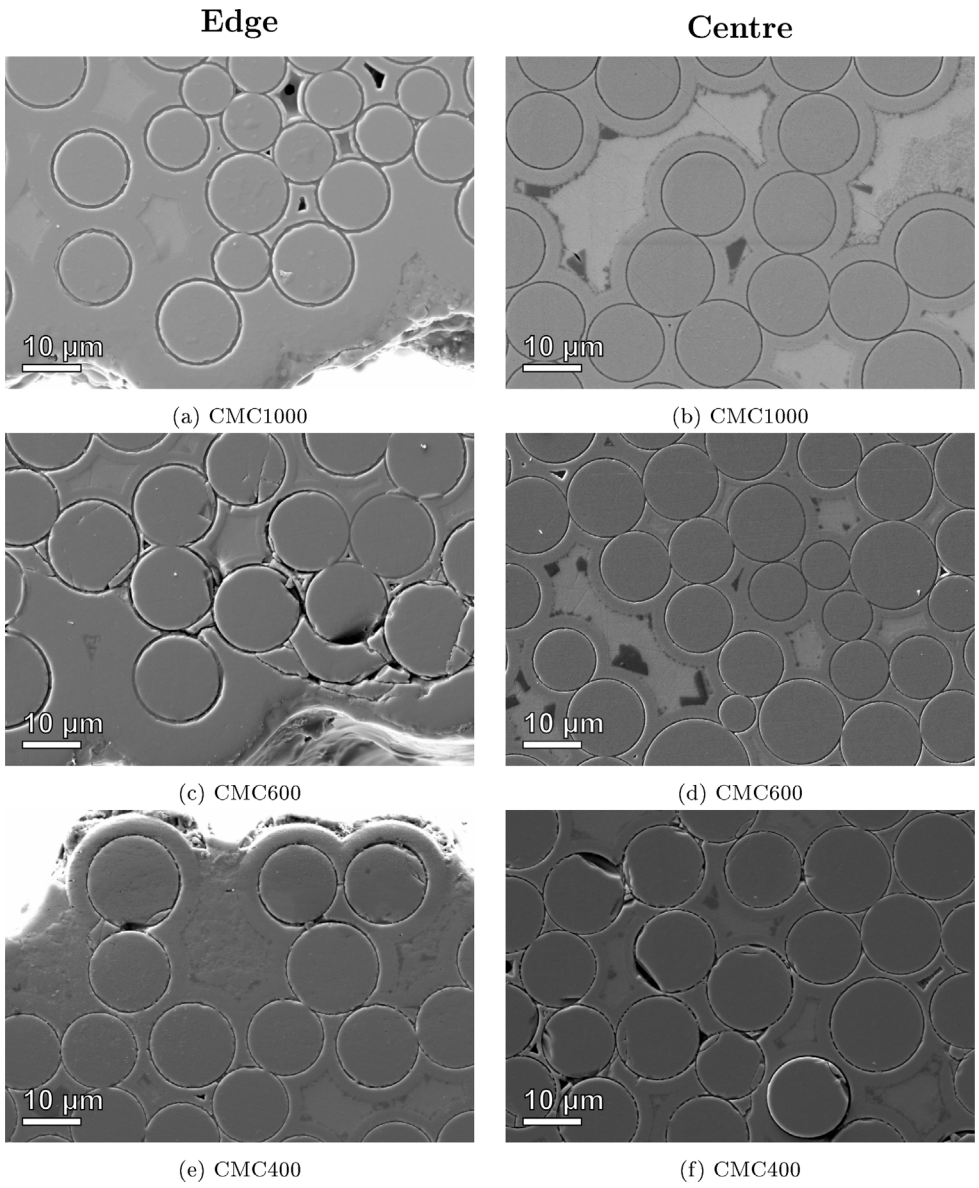

Fig. 3. SEM images of the cross sections showing the edge of the sample (the original sample surface) (a, c and e) and parts of a fibre tow from the centre of the sample (b, d and f).

fibres together see Fig. 5(a). Selected area diffraction and the EELS silicon edge from the oxide bridge show that it is amorphous silica, see Fig. 6(a) and compare to Figure S7a in the Supplementary Information. It can also be seen from the boron spectra, see Fig. 6(b), that there are small amounts of boria in the same area, indicating a borosilicate with low boron content. In general, the oxide layers of CMC1000 had detectable amounts of both silica and boria, while those of CMC600 and CMC400 showed clear signal for silica, see Fig. 6, and may have a weak boria signal, but it is too weak to properly determine if it is present, see Figs. 6(e) and 6(h). Inspecting the oxide layer in CMC600 there are features such as the one in Fig. 5(b), that have a shape similar to what one would expect from necking in a viscous fluid. This would require boria in the oxide as 600 °C is below the glass transition temperature for pure silica. The feature in Fig. 5(b) has increased amounts of boron at the edge closest to the interphase, indicating that the oxide and interphase were connected before complete separation of the surfaces.

The presence of regions of oxide between the fibres in CMC1000, not found in any other region within these samples, indicate that the oxidation is more rapid in areas where the fibres are separated by only interphase, without any CVI SiC. This has been observed before in other detailed studies on the oxidation of CMC's [34,44]. Similar features were not seen in CMC600 or CMC400, but the oxidation process in these samples was likely affected by the debonding of the interphase in these samples.

In addition to the oxide layers, the surface sample of CMC1000 has additional layers between fibre/interphase as well as CVI SiC/interphase as can be seen in Fig. 5(a) and in Figure S8 in the Supplementary Information. An HR-TEM image of the fibre/interphase region from square 2 in Fig. 4(a) can be seen in Fig. 7 and corresponding EELS edges for relevant elements can be found in Fig. 8. The layered structure in this area consists of the fibre (4), an unidentified layer (3), an oxide layer (2) and the tBN interphase (1). The turbostratic structure of the interphase is clearly lost in the oxide layer (2) and by inspecting the silicon and boron edges it can be seen that layer (2) is a layer of amorphous borosilicate. Between this layer and the fibre is a layer with slight signs of a turbostratic nature, at least locally, and from the EELS edges this area contain silica, amorphous carbon, boron nitride and boria and can be interpreted as a layer of partially oxidised remaining interphase. A similar layered structure as that along parts of the fibres was found along parts of the CVI, see Figure S8 in the

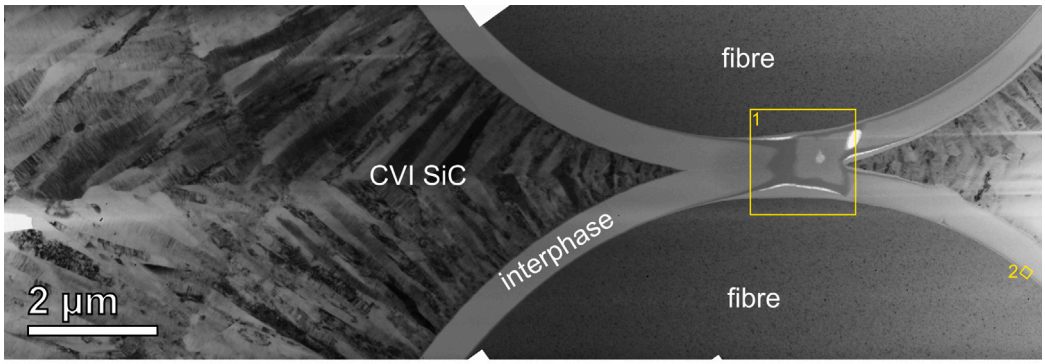

(a) Sample CMC1000

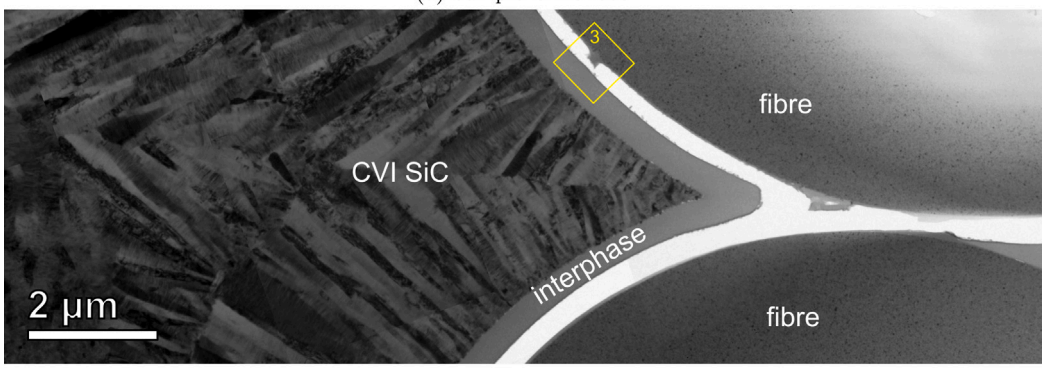

(b) Sample CMC600

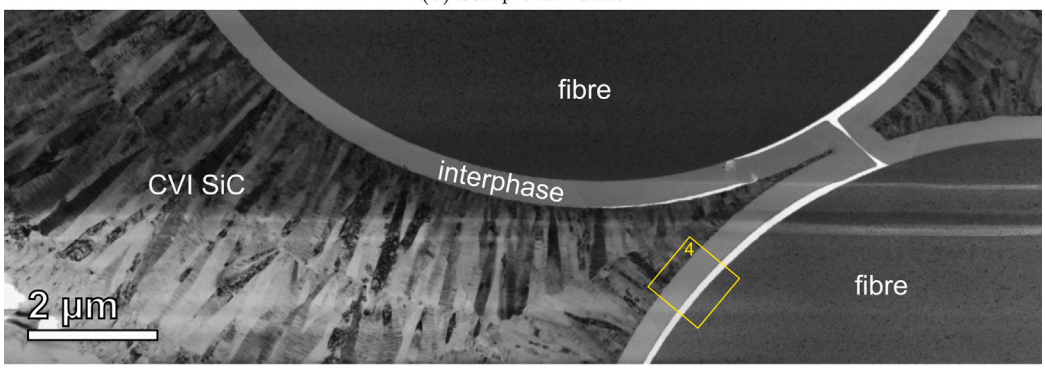

(c) Sample CMC400

Fig. 4. Bright field TEM images of the surface samples. Yellow squares show where more detailed investigations were made.

Supplementary Information. This layered structure was very similar to the one described above.

The thin layer of interphase between the fibre and oxide layer indicate that the diffusion of silicon containing species into the tBN interphase is fast enough to prevent the formation of an oxide layer directly at the surface, but instead it forms inside the interphase when the concentration gets high enough for phase separation. It is worth mentioning that from the data on the surface samples it is not possible to know if silicon diffuse into the interphase prior to or post oxidation. It is probable that the reason for having silica layers directly adjacent to the fibre in CMC600 and CMC400 is due to the cracking events that prevent further diffusion of silica into the interphase.

In some areas of sample CMC1000 there is an additional layer of carbon, see Fig. 5(a). This carbon also stretches into layers following parts of the interfaces between interphase and SiC. EELS fine structure analysis confirms that this is amorphous carbon, see Fig. 9. Similar amounts of carbon were not found in any of the other surface samples which indicate that it is not an artifact from sample preparation or surface treatment of the fibres during sample manufacturing. It is likely a result of a high oxidation rate and reaction (3), but further studies are needed to properly confirm this.

3.3.2. Remaining interphase

The boron signal from the tBN interphase of sample CMC1000, see Fig. 6(b), show that the signal is dominated by tBN, but the small shoulder at about 1.5 eV above the first peak indicate that there is also some boria in the interphase, along with silica as can be seen in the silicon spectra from the same region in Figs. 6(a) and 8(b). Both CMC600 and CMC400 also show signs of silica in the interphase, see Figs. 6(d) and 6(g), while boria could be identified in CMC600 but not clearly in CMC400, see Figs. 6(e) and 6(h). The silica in the interphase is again indicative of a diffusion of silicon containing species as a part of the oxidation process.

All samples had carbon dispersed in the interphase, see Figs. 9, 6(f) and 6(i) and compare with Figure S7c in the Supplementary Information, which has been reported previously for tBN layers deposited by CVI [45]. It is however not possible to tell if the carbon detected in this study was deposited together with the tBN or if it is contamination from sample preparation.

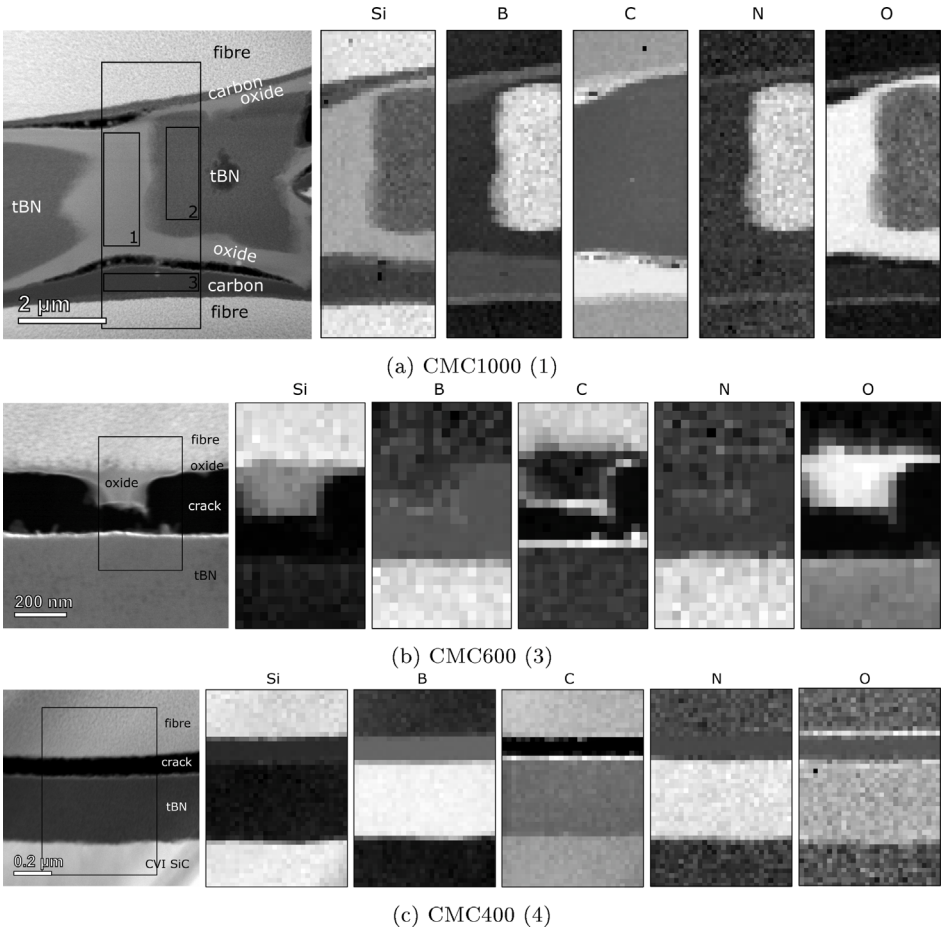

Fig. 5. Elemental maps from all samples. Numbers in parentheses show where the maps were acquired, referring to the numbering of yellow squares in Fig. 4.

3.4. (S)TEM centre samples

The centre samples reveal how the centre of the dogbone samples have been affected. CMC1000 and CMC600 show no signs of any oxide layers in the centre, see Figs. 10(a) and 10(b). The silicon spectra summed over the interphase show no signs of silicon migration for sample CMC1000 and possibly a weak signal corresponding to silica in sample CMC600, although this signal is below the noise level, see Fig. 11. From the surface samples it was not possible to discern if the silicon for the silica in the tBN interphase had diffused before or after oxidation. The centre samples were subjected to similar temperatures but without the oxidising species and no silicon, or only very little amounts in the form of silica, was found in the interphase, indicating that the oxidation happens prior to or simultaneous with the migration and temperature alone could not cause diffusion of silicon. The increased oxygen signal in the interphase seen in the maps of Figs. 10(a) and 10(b) is likely an artefact caused by differing sample thickness as no elemental edges corresponding to oxide species were identified. Overall no signs of degradation of the interphase were found in the centre sample of CMC1000, and for CMC600 the only indication of degradation was a very weak silica signal in the interphase, this is in line with what was seen in the polished cross sections and fracture surfaces and show that time is more important than temperature in order for the oxidation to reach the centre of the sample.

The centre sample of CMC400 contain a crack between the fibre and interphase, which was present before thinning, see Fig. 10(c). The different contrasts seen in the interphase stem from uneven milling and do not represent any change in composition.

A notable feature in the EELS maps of Fig. 10(c) is the oxygen rich layer on the fibre surface. The fine structure plots of Fig. 12(a) show that this region consist of silica, and this silica layer also contain boria, as seen in Fig. 12(b). A weak silica signal was also found on the other side of the crack at the edge of the interphase, and a weak silica signal can be found throughout the interphase, see Fig. 12(b). This indicates that the test conditions did enable boria formation and it is likely that boria was formed also on the surface but the proximity to the atmosphere allowed for sufficient exposure to water for volatilisation of boria according to reaction (5), which led to the lower signal in the surface samples.

Table 2
Summary of results obtained from TEM and EELS analysis. √ = Present, × = Not present, Empty = Not relevant.

	CMC1000		CMC600		CMC400	
Time to failure	27.34 h		150.11 h		2426.0 h	
	Surface	Centre	Surface	Centre	Surface	Centre
Oxide layer on fibre	√	×	√	×	√	√
Oxide thickness[a]	20–200 nm		80 nm		20 nm	10 nm
Boria in oxide	√		√		(√)	√
Oxide layer on CVI	√	×	×	×	×	×
Silica in interphase	√	×	√	×	√	(√)
Boria in interphase	√	×	√	×	×	×

[a] Approximate value, varies along the fibre circumference.

4. Summary of results and final discussion

The results are summarised in Table 2. All samples suffered oxidation of both SiC and tBN, but the extent varies with temperature.

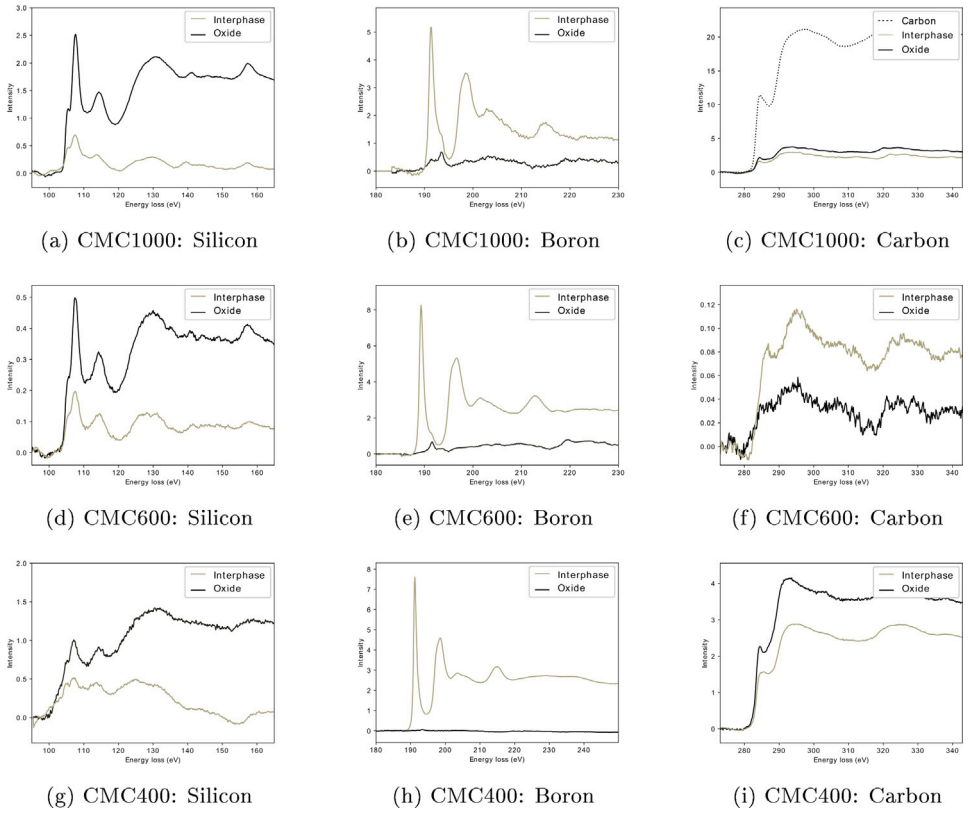

Fig. 6. Spectra from interphase and oxide layers of the surface samples of CMC1000, CMC600 and CMC400. CMC1000 spectra are from the regions marked 1 (oxide), 2 (interphase) and (3) carbon in Fig. 5(a). Spectra in (b), (e) and (g) were post-processed for background correction in Digital Micrograph.

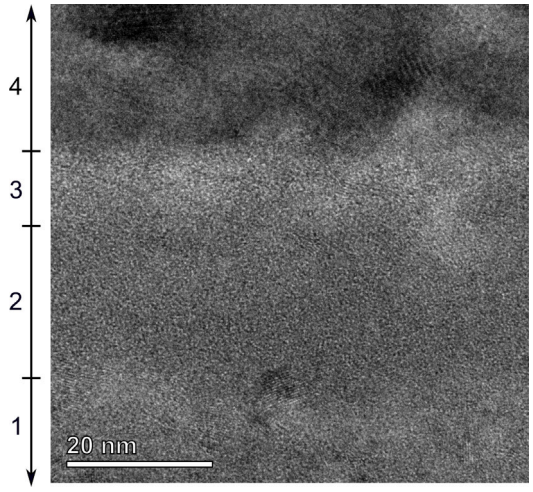

Fig. 7. HR-TEM image across the layered structure, showing fibre (4), an unknown layer (3), an amorphous oxide layer (2) and interphase (1). The image is taken from the region marked 2 in Fig. 4(a).

Sample CMC1000 experienced severe oxidation in areas close to the surface, leading to fibre fracture around the edges and transfer of load to a smaller cross section which in turn led to complete failure of the composite, this is seen both in TEM samples and SEM investigations. Sample CMC400 had much milder oxidation but it was in the test long enough for the oxidation to reach the centre of the sample and the whole composite failed simultaneously. Sample CMC600 had an appearance in between the other two.

In all samples there was still significant amounts of tBN interphase left at the moment of failure, both in the centre and close to the sample surface, thus the fibre fracture along the edges cannot be attributed to compete removal of the interphase or complete welding of fibres by oxide formation. This together with the fibre fracture seen in the polished cross sections in the same areas where oxides were found in TEM-samples indicate that the strength of the SiC fibres have decreased as a result of the oxidation. Sha et al. have reported loss of fibre strength in Hi Nicalon fibres after loading at high temperature and attributed it to nucleation of new flaws due to oxidation and loading [46], Hay and Chater reported a loss of strength in fibres after being oxidised in the presence of water vapour [47], although their work was done on Hi Nicalon type S fibres which have a lower oxygen content and less free carbon in the pristine fibre. A loss of fibre strength as a result of the oxide formation on the fibre surface is the most likely explanation for the composite failure seen in this work.

It has been seen in this work that during a tensile creep test at elevated temperature, a migration of silicon will happen alongside with oxidation. The absence of silicon in the interphase in the centre samples of CMC600 and CMC1000 show that the migration happens during or after oxidation. Silicon migration has also been seen by Opila et al.. when testing SiC/BN/SiC CMC's in burner rigs with jet fuel, and they suggested it happened due to the interaction of silicon oxidation products with boria in the interphase [13]. It was also seen by Diaz et al. in low temperature humidity tests, but in that case in the form of SiC migration followed by oxidation once the sample was heated to 800 °C [30]. At 1000 °C this migration appears to be fast enough to prevent formation of a silica layer directly adjacent to the fibre surface and instead a layer forms inside the tBN, as indicated by the presence of tBN between the silica layer and fibre surface. Layered structures were also seen by More et al. after oxygen exposure at 950 and 600 °C in the form of a layer of borosilicate formed after the silica layer had first coated the fibre [48]. Dugne et al. found layered structure along the fibre/interphase interface in the form of a carbon layer coating the fibre, followed by a silica layer before the interphase layer, already

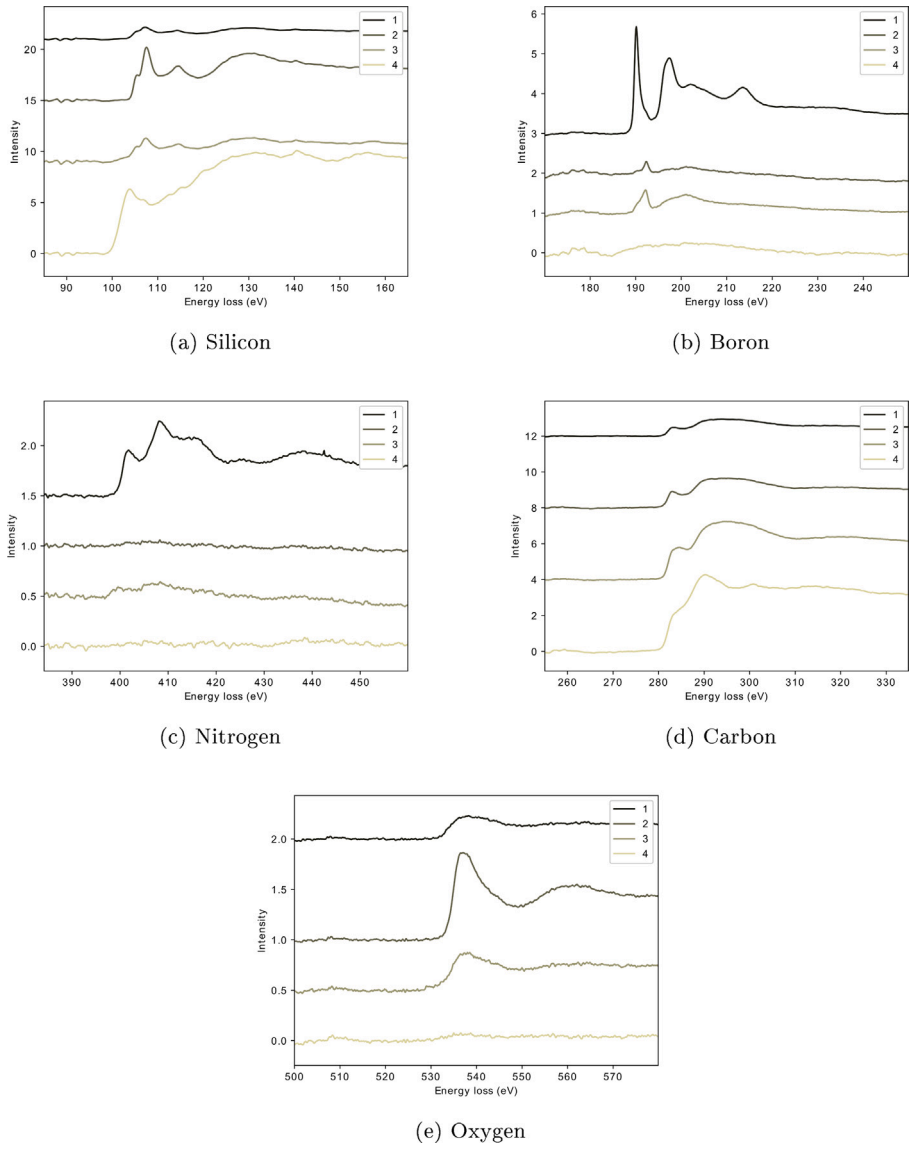

Fig. 8. Fine structure spectra across the layers in Fig. 7, showing fibre (4), an unknown layer (3), an amorphous oxide layer (2) and interphase (1).

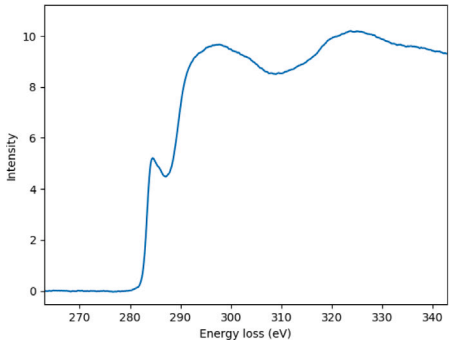

Fig. 9. Carbon edge from the area labelled (3) in Fig. 5(a).

after processing [41], their work was however based on Nicalon fibres which have higher intrinsic oxygen content than the Hi Nicalon fibres used in this work and the Nicalon fibres could form the same layers after only heating. Similar layer were seen by Sun et al. [45]. Samples CMC600 and CMC400 had silica directly adjacent to the fibres, but it is not possible to tell if this is due to the separation of fibre and interphase making silica migration impossible. The silica found in the interphase in these samples is indicative of some silica migration, either from the fibre prior to crack formation or by oxidation of the CVI SiC. The boria found in the oxide does however indicate that at least some of this oxide formed before the crack formation.

In line with previous studies the oxidation is more noticeable on the fibre/interphase than the CVI SiC/interphase interface [26,49]. At high temperatures, >1000 °C, Opila et al. found equal oxidation of fibre and CVI SiC, and also in this work significant oxidation of the CVI SiC was only seen in CMC1000. It was further seen that in sample CMC1000 the most severe oxidation was found where the fibres were closest and separated by only interphase. Similar trends were seen by Zawada et al. [40]. This welding of fibres by oxide bridges may act as crack initiation sites which in turn will start the formation of the surface cracks responsible for the "picture frame" fracture surfaces seen in this sample. In sample CMC400 both TEM lamellae had cracks between fibre and interphase, and it is likely that the composite failure happened through a continued accumulation of cracks throughout the composite.

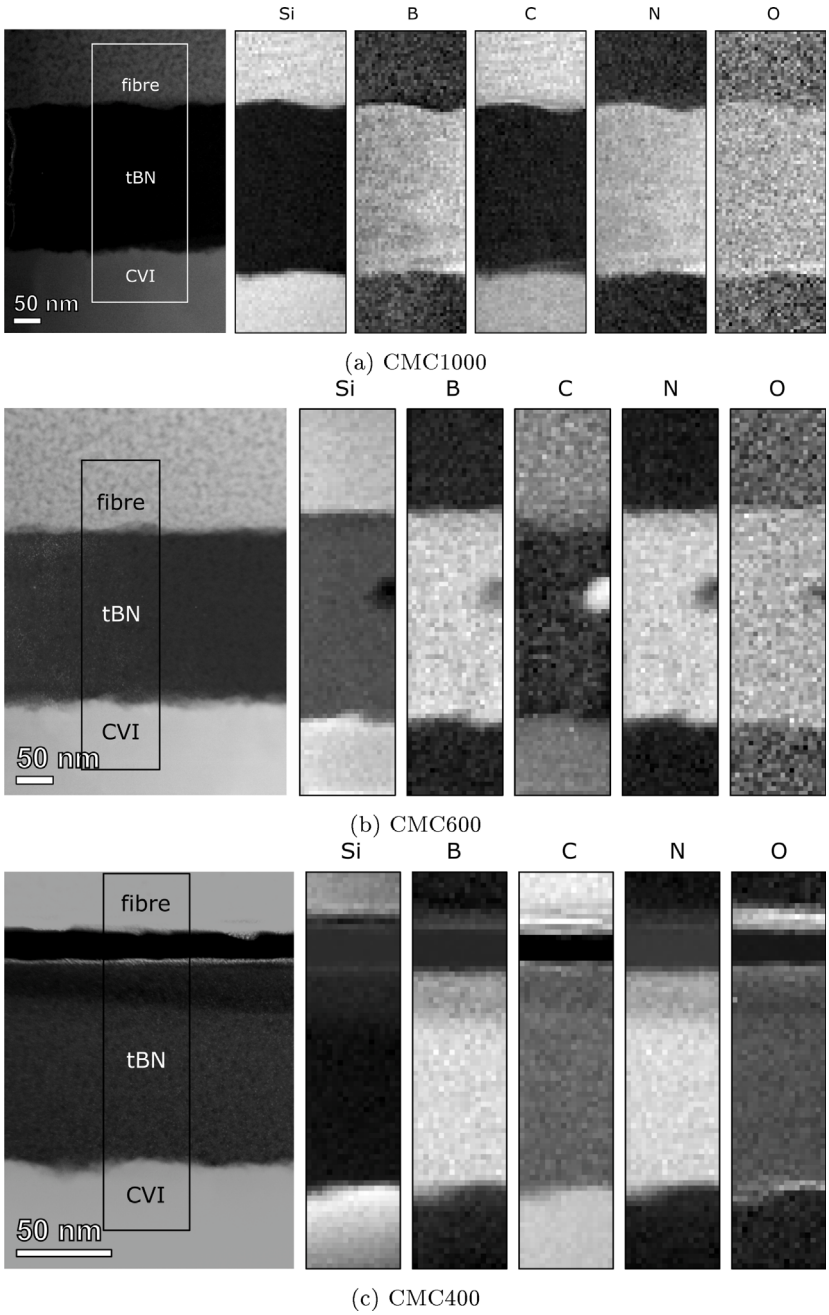

Fig. 10. EELS maps across fibre/interphase/CVI SiC for all centre samples.

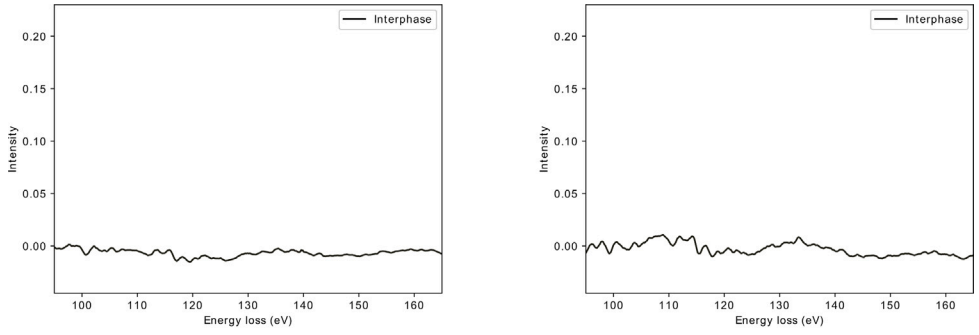

Fig. 11. Silicon spectra from the interphase of the centre samples of CMC1000 and CMC600.

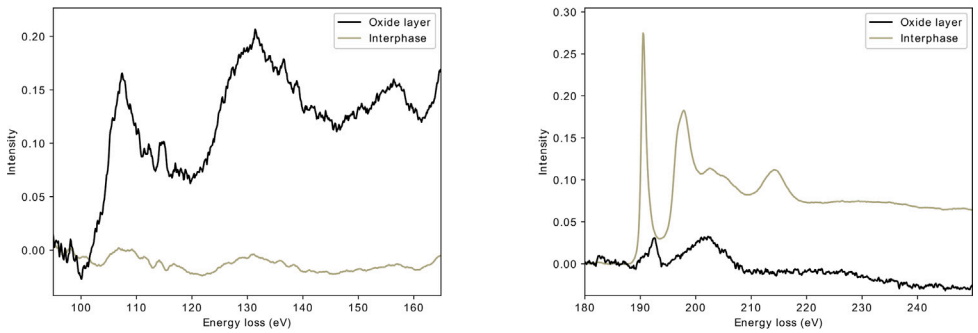

Fig. 12. Spectra from the interphase and oxide layer of the centre sample of CMC400.

5. Conclusions

This work has shown that early oxidation along the edges will lead to fibre failure at the sample surface and transfer of load, leading to complete composite failure. At lower test temperature the early degradation along the sample edges is not as severe and the degradation will have time to spread through the composite along with an accumulation of cracks leading to failure of the whole sample simultaneously. It was seen that even in the regions with the most severe degradation, significant amounts of tBN interphase was still present, which together with fibre fracture of cross sections indicate that alongside with the formation of oxidation products the fibres themselves have degraded and lost strength. It was further seen that the oxidation happens through formation of silica and boria at all tested temperatures, and that silica will migrate into the interphase. At 1000 °C this migration is fast enough to prevent formation of a silica layer directly adjacent to the fibre and CVI SiC.

CRediT authorship contribution statement

L.R.M. Toller-Nordström: Writing – original draft, Project administration, Methodology, Investigation, Formal analysis. **O. Gavalda-Diaz:** Writing – review & editing, Methodology, Investigation. **L. Gale:** Writing – review & editing, Methodology, Funding acquisition, Conceptualization. **D.E.J. Armstrong:** Writing – review & editing, Supervision, Funding acquisition, Conceptualization. **R.J. Nicholls:** Writing – review & editing, Supervision, Methodology, Funding acquisition, Formal analysis, Conceptualization.

Declaration of competing interest

The authors declare the following financial interests/personal relationships which may be considered as potential competing interests: Lisa Toller-Nordström and Oriol Gavalda-Diaz have received funding from Rolls Royce plc. to carry out their work. Louise Gale is employed by Rolls Royce plc.

Acknowledgements

This work was funded by Rolls Royce plc.. R. J. Nicholls would like to acknowledge funding from the EBSRC (EP/LP022907/1). The authors would also like to acknowledge the use of microscopes accessed through the David Cockayne Centre for Electron Microscopy, Department of Materials, University of Oxford.

Appendix A. Supplementary data

Supplementary material related to this article can be found online at https://doi.org/10.1016/j.jeurceramsoc.2024.117039.

References

[1] R. Naslain, Design, preparation and properties of non-oxide CMCs for application in engines and nuclear reactors: an overview, Compos. Sci. Technol. 64 (2) (2004) 155–170.
[2] J.A. DiCarlo, Advances in SiC/SiC composites for aero-propulsion, in: Ceramic Matrix Composites: Materials, Modeling and Technology, Wiley Online Library, 2014, pp. 217–235.
[3] M. Fellet, W. Rossner, Ceramic-matrix composites take the heat, MRS Bull. 40 (11) (2015) 916–918.
[4] J. Steibel, Ceramic matrix composites taking flight at GE aviation, Am. Ceram. Soc. Bull. 98 (3) (2019) 30–33.
[5] D. Marshall, B.N. Cox, A.G. Evans, The mechanics of matrix cracking in brittle-matrix fiber composites, Acta Metall. 33 (11) (1985) 2013–2021.
[6] R. Naslain, O. Dugne, A. Guette, J. Sevely, C.R. Brosse, J.-P. Rocher, J. Cotteret, Boron nitride interphase in ceramic-matrix composites, J. Am. Ceram. Soc. 74 (10) (1991) 2482–2488.
[7] A.G. Evans, Ceramics and ceramic composites as high-temperature structural materials: Challenges and opportunities, Philos. Trans. R. Soc. Lond. Ser. A Math. Phys. Eng. Sci. 351 (1697) (1995) 511–527.
[8] R. Naslain, Ceramic matrix composites, Philos. Trans. R. Soc. Lond. Ser. A Math. Phys. Eng. Sci. 351 (1697) (1995) 485–496.
[9] A. Evans, The mechanical properties of reinforced ceramic, metal and intermetallic matrix composites, Mater. Sci. Eng. A 143 (1–2) (1991) 63–76.
[10] L. Filipuzzi, G. Camus, R. Naslain, J. Thebault, Oxidation mechanisms and kinetics of 1D-SiC/c/SiC composite materials: I, An experimental approach, J. Am. Ceram. Soc. 77 (2) (1994) 459–466.
[11] B.W. Sheldon, E.Y. Sun, S.R. Nutt, J.J. Brennan, Oxidation of BN-coated SiC fibers in ceramic matrix composites, J. Am. Ceram. Soc. 79 (2) (1996) 539–543.
[12] N.S. Jacobson, G.N. Morscher, D.R. Bryant, R.E. Tressler, High-temperature oxidation of boron nitride: II, boron nitride layers in composites, J. Am. Ceram. Soc. 82 (6) (1999) 1473–1482.
[13] E.J. Opila, R.C. Robinson, M.J. Verrilli, Borosilicate glass-induced fiber degradation of SiC/BN/SiC composites exposed in combustion environments, Int. J. Appl. Ceram. Technol. 13 (3) (2016) 434–442.
[14] N.S. Jacobson, D.S. Fox, E.J. Opila, High temperature oxidation of ceramic matrix composites, Pure Appl. Chem. 70 (2) (1998) 493–500.
[15] R. Hay, G. Fair, R. Bouffioux, E. Urban, J. Morrow, A. Hart, M. Wilson, Hi-NicalonTM-S SiC fiber oxidation and scale crystallization kinetics, J. Am. Ceram. Soc. 94 (11) (2011) 3983–3991.
[16] M. Wilson, E. Opila, A review of SiC fiber oxidation with a new study of Hi-Nicalon SiC fiber oxidation, Adv. Eng. Mater. 18 (10) (2016) 1698–1709.
[17] N. Jacobson, S. Farmer, A. Moore, H. Sayir, High-temperature oxidation of boron nitride: I, monolithic boron nitride, J. Am. Ceram. Soc. 82 (2) (1999) 393–398.
[18] S. Lee, J. Stebbins, Extent of intermixing among framework units in silicate glasses and melts, Geochim. Cosmochim. Acta 66 (2) (2002) 303–309.
[19] M.F. Yan, J.B. MacChesney, S.R. Nagel, W. Rhodes, Sintering of optical wave-guide glasses, J. Mater. Sci. 15 (1980) 1371–1378.
[20] T. Furukawa, W.B. White, Raman spectroscopy of heat-treated B2o3-SiO2 glasses, J. Am. Ceram. Soc. 64 (8) (1981) 443–447.
[21] S. Sakka, J. Mackenzie, Relation between apparent glass transition temperature and liquids temperature for inorganic glasses, J. Non-Cryst. Solids 6 (2) (1971) 145–162.
[22] J. Schlichting, Oxygen transport through glass layers formed by a gel process, J. Non-Cryst. Solids 63 (1–2) (1984) 173–181.
[23] K.L. More, P.F. Tortorelli, L.R. Walker, N. Miriyala, J.R. Price, M. van Roode, High-temperature stability of SiC-based composites in high-water-vapor-pressure environments, J. Am. Ceram. Soc. 86 (8) (2003) 1272–1281.
[24] B. McFarland, E.J. Opila, Silicon carbide fiber oxidation behavior in the presence of boron nitride, J. Am. Ceram. Soc. 101 (12) (2018) 5534–5551.

[25] L. Quemard, F. Rebillat, A. Guette, H. Tawil, C. Louchet-Pouillerie, Self-healing mechanisms of a SiC fiber reinforced multi-layered ceramic matrix composite in high pressure steam environments, J. Eur. Ceram. Soc. 27 (4) (2007) 2085–2094.
[26] V.L. Christensen, F.W. Zok, Insights into internal oxidation of SiC/BN/SiC composites, J. Am. Ceram. Soc. 106 (2) (2023) 1561–1575.
[27] S. Johnson, R. Brittain, R. Lamoreaux, D. Rowcliffe, Degradation mechanisms of silicon carbide fibers, J. Am. Ceram. Soc. 71 (3) (1988) C–132.
[28] T. Matsuda, N. Uno, H. Nakae, T. Hirai, Synthesis and structure of chemically vapour-deposited boron nitride, J. Mater. Sci. 21 (1986) 649–658.
[29] S. Mall, K. LaRochelle, Fatigue and stress-rupture behaviors of SiC/SiC composite under humid environment at elevated temperature, Compos. Sci. Technol. 66 (15) (2006) 2925–2934.
[30] O.G. Diaz, K. Marquardt, S. Harris, L. Gale, L. Vandeperre, E. Saiz, F. Giuliani, Degradation mechanisms of SiC/BN/SiC after low temperature humidity exposure, J. Eur. Ceram. Soc. 40 (12) (2020) 3863–3874.
[31] R.M. De Meyere, L. Gale, S. Harris, I. Edmonds, A.L. Chamberlain, T.J. Marrow, D.E. Armstrong, Micromechanical properties of vapour-exposed SiCf/BN/SiC ceramic-matrix composites, J. Eur. Ceram. Soc. 42 (7) (2022) 3148–3155.
[32] J. Brennan, Interfacial characterization of a slurry-cast melt-infiltrated SiC/SiC ceramic-matrix composite, Acta Mater. 48 (18–19) (2000) 4619–4628.
[33] D. Bertrand, V. Sabelkin, L. Zawada, S. Mall, Fatigue behavior of sylramic-iBN/BN/CVI SiC ceramic matrix composite in combustion environment, J. Mater. Sci. 50 (2015) 7437–7447.
[34] L.U. Ogbuji, A pervasive mode of oxidative degradation in a SiC-SiC composite, J. Am. Ceram. Soc. 81 (11) (1998) 2777–2784.
[35] G.N. Morscher, Tensile stress rupture of SiCf/SiCmMinicomposites with carbon and boron nitride interphases at elevated temperatures in air, J. Am. Ceram. Soc. 80 (8) (1997) 2029–2042.
[36] T.T. Kim, S. Mall, L.P. Zawada, G. Jefferson, Simultaneous fatigue and combustion exposure of a SiC/SiC ceramic matrix composite, J. Compos. Mater. 44 (25) (2010) 2991–3016.
[37] Y. Ikarashi, T. Ogasawara, T. Aoki, Effects of cyclic tensile loading on the rupture behavior of orthogonal 3-D woven SiC fiber/SiC matrix composites at elevated temperatures in air, J. Eur. Ceram. Soc. 39 (4) (2019) 806–812.
[38] L. Porte, A. Sartre, Evidence for a silicon oxycarbide phase in the Nicalon silicon carbide fibre, J. Mater. Sci. 24 (1989) 271–275.
[39] S. Dong, G. Chollon, C. Labrugere, M. Lahaye, A. Guette, J. Bruneel, M. Couzi, R. Naslain, D. Jiang, Characterization of nearly stoichiometric SiC ceramic fibres, J. Mater. Sci. 36 (2001) 2371–2381.
[40] L.P. Zawada, J. Staehler, S. Steel, Consequence of intermittent exposure to moisture and salt fog on the high-temperature fatigue durability of several ceramic-matrix composites, J. Am. Ceram. Soc. 86 (8) (2003) 1282–1291.
[41] O. Dugne, S. Prouhet, A. Guette, R. Naslain, R. Fourmeaux, Y. Khin, J. Sevely, J. Rocher, J. Cotteret, Interface characterization by TEM, AES and SIMS in tough SiC (ex-PCS) fibre-SiC (CVI) matrix composites with a BN interphase, J. Mater. Sci. 28 (1993) 3409–3422.
[42] F.E. Heredia, J.C. McNulty, F.W. Zok, A.G. Evans, Oxidation embrittlement probe for ceramic-matrix composites, J. Am. Ceram. Soc. 78 (8) (1995) 2097–2100.
[43] A.G. Evans, F.W. Zok, R.M. McMeeking, Z.Z. Du, Models of high-temperature, environmentally assisted embrittlement in ceramic-matrix composites, J. Am. Ceram. Soc. 79 (9) (1996) 2345–2352.
[44] G.N. Morscher, J.Z. Gyekenyesi, R.T. Bhatt, Damage accumulation in 2-D woven SiC/SiC ceramic matrix composites, in: ASTM Special Technical Publication, Vol. 1392, AMERICAN TECHNICAL PUBLISHERS LTD, 2000, pp. 306–320.
[45] E.Y. Sun, S.R. Nutt, J.J. Brennan, Interfacial microstructure and chemistry of SiC/BN dual-coated nicalon-fiber-reinforced glass-ceramic matrix composites, J. Am. Ceram. Soc. 77 (5) (1994) 1329–1339.
[46] J. Sha, J. Park, T. Hinoki, A. Kohyama, Tensile properties and microstructure characterization of Hi-Nicalon TM SiC fibers after loading at high temperature, Int. J. Fract. 142 (2006) 1–8.
[47] R.S. Hay, R.J. Chater, Oxidation kinetics strength of Hi-NicalonTM-S SiC fiber after oxidation in dry and wet air, J. Am. Ceram. Soc. 100 (9) (2017) 4110–4130.
[48] K. More, K. Ailey, R. Lowden, H. Lin, Evaluating the effect of oxygen content in BN interfacial coatings on the stability of SiC/BN/SiC composites, Composites A 30 (4) (1999) 463–470.
[49] F.W. Zok, P.T. Maxwell, K. Kawanishi, E.B. Callaway, Degradation of a SiC-SiC composite in water vapor environments, J. Am. Ceram. Soc. 103 (3) (2020) 1927–1941.